ORIGINAL PAPER

Protic ionic liquid-based gel polymer electrolyte: structural and ion transport studies and its application in proton battery

Kuldeep Mishra · S. A. Hashmi · D. K. Rai

Abstract Proton-conducting free standing gel polymer electrolyte (GPE) films containing protic ionic liquid, 1-butyl-3-methylimidazolium hydrogen sulphate, immobilized in blend of poly(vinylidenefluoride-co-hexafluoropropylene) and poly(vinylpyrrolidone) have been prepared by solution-cast technique. Films have been characterized by Fourier transform infrared spectroscopy (FTIR), X-ray diffraction (XRD), scanning electron microscope (SEM), differential scanning calorimetry (DSC), complex impedance spectroscopy, and cyclic voltammetry. Ionic conductivity of the semicrystalline and porous GPE films has been obtained as ~3.9×10^{-3} S cm^{-1} at room temperature. Protonic nature of conduction in the films has been established by performing cyclic voltammetry and complex impedance spectroscopy on the cells having both blocking (stainless steel) and both reversible electrodes (Zn + ZnSO$_4$.7H$_2$O). The electrochemical stability window of the films has been found as ~3.8 V. The highest conducting film has been used as a separator and proton conductor to fabricate a proton battery of configuration Zn + ZnSO$_4$.7H$_2$O |GPE film| PbO$_2$ + V$_2$O$_5$. The battery shows an open circuit voltage of ~1.62 V. Energy density of the cell has been obtained as 35.2 W h kg^{-1} for low current drain. Rechargeability of the cell has been tested for ten cycles. The maximum discharge capacity of the cell has been obtained as ~2.50 mA h g^{-1} during the first discharge cycle.

Keywords Polymer electrolyte · Proton conduction · Proton battery

K. Mishra · D. K. Rai (✉)
Department of Physics and Materials Science and Engineering,
Jaypee Institute of Information Technology, Noida 201307, India
e-mail: dk.rai@jiit.ac.in

S. A. Hashmi
Department of Physics and Astrophysics, Delhi University, Delhi,
India

Introduction

In the last few years, gel polymer electrolytes (GPEs) have received considerable attention for their applications in various electrochemical devices like rechargeable batteries, fuel cells, dye-sensitized solar cells, supercapacitors, etc. particularly because of their high ionic conductivity (10^{-4} to 10^{-2} S cm^{-1}). Such electrolytes are obtained by immobilizing salt solutions (prepared in polar liquids) or ionic liquid in a polymer host like poly(vinylidenefluoride) (PVdF), poly(vinylidenefluoride-co-hexafluoropropylene) (PVdF-HFP), poly(vinyl alcohol) (PVA), poly(methyl methacrylate) (PMMA), poly(ethylene oxide) (PEO), etc., but good GPEs carry a large volume of entrapped liquid electrolyte; therefore, they suffer from dimensional instability and leakage of liquid electrolytes from their matrix which poses limitation to their applicability in electrochemical devices. For long-term electrochemical applications, polymer hosts should have mechanically and thermally stable framework that can retain the entrapped liquid electrolyte during storage and operation of electrochemical devices [1, 2]. In order to improve the properties of GPE films, addition of nano-sized ceramic fillers like MgO, SiO$_2$, Al$_2$O$_3$, ZrO$_2$, etc. into the GPE matrix has been attempted. The resulting nanocomposite GPEs have been shown to have enhanced mechanical and ion transport properties through filler–polymer and ion–polymer-filler interactions [3–5].

Apart from nanocomposites, using polymer blends as a host for GPEs has been another promising approach to address the issue of mechanical and thermal instabilities. Blending is a simple, cost effective, and low-temperature process of physically mixing two or more polymers which provides opportunity to maneuver various properties of a blend by suitably choosing the concentration of participating polymers so as to obtain a suitable host for GPE [6].

Chen and Hong [7] have studied blending of PVdF and poly(vinylpyrrolidone) (PVP) and have shown that

constituents interact through hydrogen bonding between methylene group (CH_2) of PVdF with the carbonyl group ($C = O$) of PVP. The blend has been found to have superior mechanical strength and hydrophilicity as compared to the constituents. PVdF shows high compatibility with the polymers containing oxygen in their chains [8]. Qiao et al. [9] have shown that PVP hinders the crystallization of PVdF in their blend and improves film's oxidative property and chemical stability. Wang and Tang [10] have studied lithium-ion conducting GPE based on a blend of PVdF-HFP/PVP for lithium-ion battery. They have found that PVdF-HFP/PVP blend taken as host contained porous network where pore density increased with PVP concentration. Ionic conductivity of the polymer electrolyte has been reported as $\sim 10^{-3}$ S cm^{-1}.

In the last few years, ionic liquids (ILs) have been extensively studied as electrolyte materials for their applications in various electrochemical devices like batteries, fuel cells, supercapacitors, etc. ILs are the molten salts ($T_m < 100\ ^\circ C$) with high ionic conductivity, wide liquid phase range, non-flammability, negligible vapor pressure, and better thermal and electrochemical stability [11], which specifically make them attractive electrolyte materials. The protic ionic liquids (PILs) belong to a group of ILs which manifests proton conduction. There are several excellent reviews and reports published on PILs describing their physicochemical properties. A few recent ones to mention are by Ohno [11], Greaves and Drummond [12], Anouti et al. [13], Johnson et al. [14], and Nakamoto et al. [15]. In the last few years, by immobilizing PILs as a solvating media and/or proton-conducting component in polymer matrix, many excellent polymer electrolytes have been developed [16–19]. These films have been found to show ionic conductivity as high as $\sim 10^{-2}$ S cm^{-1}. In general, both cations and anions contribute to the total conductivity of the polymer electrolytes. However, anions, being smaller in size, are supposed to have higher mobility than cations which are larger in size. Recently, Ogihara et al. [16] have studied few PILs consisting of alkylimidazolium cations, like 1-methylimidazolium, 1-ethylimidazolium, and 1-ethyl-3-methylimidazolium and multivalent anions, like HSO_4^-, $H_2PO_3^-$, $H_2PO_4^-$, and $H_3P_2O_7^-$, as proton-conducting ILs. The multivalent anions of these PILs contain hydrogen cation inherently, which are understood to contribute to proton conductivity. They have also shown that the PILs containing HSO_4^- anion have lower glass transition temperature, high ionic conductivity ($\sim 10^{-3}$ S cm^{-1}), and higher decomposition temperature as compared to other anions they had chosen.

In the present paper, we report preparation and characterization of PVdF-HFP/PVP blend-based proton-conducting GPE film immobilized with a PIL, 1-butyl-3-methylimidazolium hydrogen sulphate (BMImHSO$_4$) which contains 1-butyl-3-methylimidazolium cation (BMIm$^+$), and HSO_4^- anion, similar to the proton-conducting ILs studied by

Ogihara et al. [16]. An optimized composition, 90 wt% PVdF-HFP/10 wt% PVP, of the blend has been chosen as host for preparing GPE films. Ninety weight percent PVdF-HFP/10 wt% PVP has been referred as "blend" and 90 wt% PVdF-HFP/10 wt% PVP + x PIL as "GPE" in the following text of the paper. The paper discusses structural, thermal, and ionic conductivity studies of the GPE films.

Our group has recently undertaken systematic research on development of proton batteries using proton-conducting polymer electrolyte films as separator membrane and ion conductor. Recently, we have reported performance studies of proton battery using nanocomposite GPE film of PVdF-HFP/PMMA + SiO_2 + NH_4SCN + EC + PC as separator membrane and electrolyte and $Zn + ZnSO_4.7H_2O/PbO_2 + V_2O_5$ as cathode/anode [5]. In the present work, we have used 90 wt% PVdF-HFP/10 wt% PVP + x PIL GPE film as separator membrane and electrolyte and have carried out performance studies of the proton battery. To the best of our knowledge, no proton battery has yet been reported using PIL-based polymer electrolyte as electrode separator.

Experimental

Materials and film preparation

The polymers, PVdF-HFP (MW = 4×10^5) and PVP (MW = 5×10^6) and PIL, BMImHSO$_4$ (purity $\geq$94.5 %), were procured from Aldrich. Water-free common solvent dimethylformamide (DMF) of 99.9 % purity was obtained from SRL, India. These chemicals were used as received.

Films of PVdF-HFP, pure blend and blend + x PIL (GPE) for x=50, 60, and 70 wt% were prepared by solution cast technique. PVdF-HFP, PVP, and PIL were mixed in desired ratios in DMF and stirred for ~12 h at 60 °C to obtain a homogeneous viscous solution. The solution was poured into glass Petri dish and dried for ~48 h in an oven maintained at 70 °C (slightly above the flash point of DMF) to obtain solution-cast films. This process resulted into flexible, nearly transparent and free-standing films of thickness ~300–400 µm. Complete removal of DMF after drying was confirmed by Fourier transform infrared spectroscopy (FTIR) of the films.

Characterization

The FTIR spectra of films of different compositions were recorded using FTIR spectrophotometer (PerkinElmer, Spectrum BS) in ATR mode in the wave number range 650–4,000 cm^{-1}. The X-ray diffraction (XRD) patterns of different polymer films were obtained using X-ray diffractometer (SHIMADZU, XRD-6000) with Cu Kα radiation in the Bragg angle range 2θ = 5–70°. The surface morphology of the

polymer films was obtained using scanning electron microscope (SEM, LEO 435 VP). Images were taken under low vacuum after gold coating on the film surface. Differential scanning calorimetry (DSC) of different polymer films was carried out by TA instruments (Q200) at a heating rate of 10 °C min^{-1}. Ionic conductivity (σ) of GPE films was determined by complex impedance spectroscopy using NumetriQ frequency response analyzer (Model PSM1735, Newtons4th). Films were sandwiched between two blocking electrodes of stainless steel (SS) of 1 cm^2 surface area. An ac voltage of 10 mV was applied across the cell, SS |GPE film| SS and real and imaginary parts of the impedance (Z' and Z'') were measured over the frequency range 60 Hz–100 kHz. Bulk impedance of films was evaluated from the complex impedance plots drawn between Z' and Z''. Electrochemical stability window (ESW) of GPE films was determined by cyclic voltammetry (CV) using electrochemical analyzer (CH Instruments, 608C). The measurement was performed with a scan rate of 5 mV s^{-1} on the cell SS |GPE film| SS. In order to establish proton conduction in the prepared GPE films, we have carried out comparative CV and complex impedance measurements on symmetrical cells, SS |GPE film| SS, and Zn + ZnSO$_4$.7H$_2$O |GPE film| Zn + ZnSO$_4$.7H$_2$O using electrochemical analyzer (CH Instruments, 608D). The SS and Zn + ZnSO$_4$.7H$_2$O were taken as blocking and reversible electrodes respectively. The CV was carried out at different scan rates, and the complex impedance measurement was carried out in the frequency range 0.1 Hz–100 kHz.

Battery fabrication and characterization

Proton battery was fabricated using GPE film with highest ionic conductivity as separator membrane between anode and cathode. For anode, zinc dust (Zn, SRL, India) and zinc sulphate (ZnSO$_4$.7H$_2$O, Qualigens, India) were mixed in 3:1 w/w ratio and grinded to obtain a homogeneous mixture. Mixture was then pressed in the form of pellet of thickness ~0.70 mm. The above composition of zinc metal and hydrated zinc sulphate has been used as anode in several proton batteries [5, 20–27]. Oxidation of Zinc metal provides electrons in the external circuit while hydrated zinc sulphate acts as a proton (H$^+$) source during discharge cycle of the cell (half cell reaction is given in the discussion part by Eq. 3). For cathode, lead oxide (PbO$_2$, CDH, India), vanadium pentaoxide (V$_2$O$_5$, SRL, India), graphite (CDH, India), and the prepared GPE were mixed in 8:2:1:0.5 w/w ratio and grinded thoroughly. Mixture was pressed in the form of thin pellets of ~0.70 mm thickness. The constituents of the cathode, except electrolyte, and their compositions were chosen to be same as used by Pratap et al. [21] and Pandey et al. [22]. Pandey et al. [22] have studied the cathode in detail and established that apart from having a good intercalating property, it shows optimal electronic conductivity for the above composition. GPE film was

sandwiched between anode and cathode pellets and compacted in the form of a button-shaped battery of the configuration Zn + ZnSO$_4$.7H$_2$O |GPE film| PbO$_2$ + V$_2$O$_5$. The open circuit voltage (OCV) and the discharge characteristics of the proton battery were measured by Keithley 2000 multimeter. The battery was discharged through 10 kΩ, 100 kΩ, and 1 MΩ fixed load resistances. Charge/discharge characteristics of the battery were studied using battery tester (BT-2000, Arbin Instrument, USA). The battery was also subjected to the cyclic voltammetry using the electrochemical analyzer (CH instruments, 608C).

Results and discussion

FTIR studies

FTIR is an important technique which probes a material at molecular level. The unique vibrational bands of FTIR spectra result from vibrational motions of individual bond or groups in a molecule. Any change, therefore, occurring in the bonding situations of molecules results in the change in vibrational frequency. FTIR studies of the GPE films in our case are used to understand interaction/complexation between the blend host and the PIL. FTIR spectra of the pure blend film, pure PIL and GPE films of different compositions are shown in Fig. 1. Positions of the prominent characteristic bands appearing in the spectra are listed in Table 1 along with their assignments.
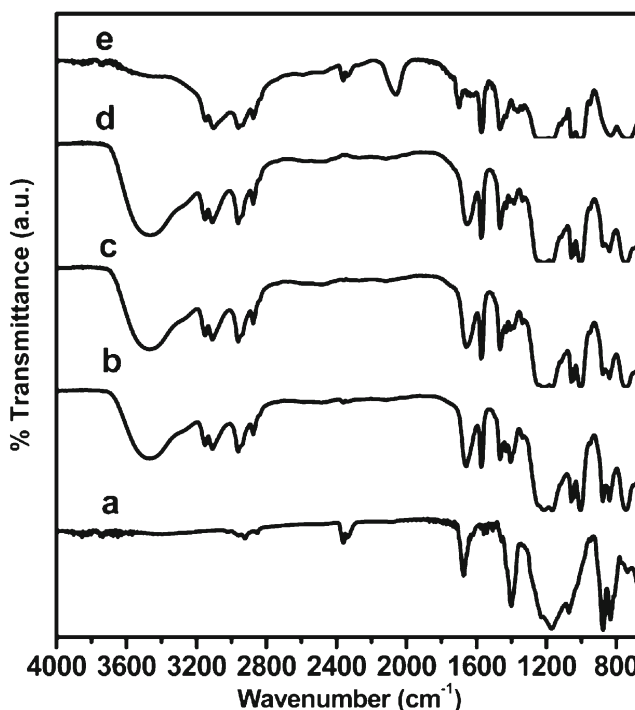

Fig. 1 FTIR spectra of the films of pure PVdF-HFP/PVP blend (**a**), PVdF-HFP/PVP+x wt% BMImHSO$_4$ with x=50 (**b**), 60 (**c**), and 70 (**d**) and pure BMImHSO$_4$ (**e**)

Table 1 FTIR band assignments of PVdF-HFP/PVP blend, PVdF-HFP/PVP + x BMImHSO$_4$ GPE, and pure BMImHSO$_4$ PIL

PVdF-HFP/PVP Blend	Blend+ 50 wt% PIL	Blend+ 60 wt% PIL	Blend+ 70 wt% PIL	Assignments [28–33]
2,960	2,960	2,960	2,960	Asymmetric CH$_2$ wagging of PVP ring
2,918	–	–	–	Symmetric CH$_2$ stretching of PVP chain
2,090	–	–	–	C-N stretching of PVP
1,675	1,660	1,656	1,651	C = O stretching of PVP
1,400	1,405	1,405	1,405	CH$_2$ wagging of PVdF-HFP/PVP
1,164	1,164	1,164	1,164	CF$_2$ antisymmetric stretching of PVdF-HFP
1,072	–	–	–	CF$_3$ out of plane deformation of PVdF-HFP
876	879	897	879	γ Phase of PVdF-HFP
834	841	841	841	γ Phase of PVdF-HFP
1,229, 812, 774	–	–	–	α phase of PVdF-HFP
PIL (BMImHSO$_4$)				
3,473	3,473	3,473	3,473	–OH group of adsorbed water
3,152	3,152	3,152	3,152	C(2)-H stretching
3,103	3,109	3,109	3,111	HC(4)-C(5)H antisymmetric and symmetric vibration of imidazolium ring
2,963	2,963	2,963	2,963	Symmetric stretching of butyl chain
2,935	2,935	2,935	2,935	Fermi resonance of CH$_3$ attached with butyl chain
2,875	2,875	2,875	2,875	Symmetric stretching mode of CH$_3$ attached with butyl chain
2,059	–	–	–	Unassigned
1,704	1,660	1,656	1,651	Imidazolium ring combination band
1,573	1,573	1,573	1,573	C-C, C-N stretching
1,465	1,465	1,465	1,465	Out of plane vibration of imidazolium ring
1,210 (Broad)	1,210	1,210	1,210	SO$_3$ antisymmetric stretching
1,059	1,059	1,059	1,059	Inner plane asymmetric stretching of imidazolium ring
1,046	1,046	1,046	1,046	Symmetric stretching of imidazolium ring and HSO$_4^-$ stretching vibrations
1,006	1,006	1,006	1,006	In-plane wagging of butyl chain
832	–	–	–	In-plane imidazolium ring bending
735	745	746	748	C-H wagging vibrations of imidazolium ring

The prepared GPE films consist of blend of PVdF-HFP and PVP as host and BMImHSO$_4$ as electrolyte. As PVP is a highly polar polymer possessing carbonyl group (C = O), it is able to form complex with imidazolium cation of PIL. Therefore, we may expect change in the characteristic bands of carbonyl groups as well as bands related with imidazolium ring of PIL. Further, being a highly polar medium, BMImHSO$_4$ is capable of affecting the crystalline phases of the blend. Therefore, we may expect change in the bands related with different crystalline phases of PVdF-HFP.

The complexation of PVP with imidazolium cation is confirmed by gradual shifting of C = O stretching band from 1,675 cm^{-1} in the spectrum of blend film to 1,660, 1,656, and 1,651 cm^{-1} in the spectra of GPE films with PIL concentration 50, 60 and 70 wt% respectively as shown in Table 1. Changes in several bands of PIL have also been observed which have

been attributed to its complexation with PVP. The band at 3,103 cm^{-1} corresponding to HC(4)-C(5)H antisymmetric and symmetric vibration of imidazolium ring shifts to 3,109 cm^{-1} in the GPE system. Other bands appearing at 1,704 and 735 cm^{-1} for combination band and C-H wagging of imidazolium ring gradually shift in GPE with addition of PIL. Disappearance of bands at 2,059 cm^{-1} (unassigned) and 735 cm^{-1} for in-plane imidazolium ring bending of PIL has also been observed in the spectra of GPE.

PVdF-HFP, the other polymer constituent of prepared GPE films, has two most commonly observed crystalline phases namely intermediate polar γ phase having *TTTGTTTG*' conformation and nonpolar α phase having trans-gauche-trans-gauche' (*TGTG*') conformation [28]. Bands at 876 and 834 cm^{-1} and 1,229, 812, and 774 cm^{-1} in the spectra of pure blend film confirm the presence of both the crystalline phases

in the pure blend. The former two bands correspond to γ phase and later three bands correspond to α phase of PVdF-HFP. It is observed that in the spectra of GPE films, bands of γ phase shift to 879 and 841 cm^{-1} while bands of α phase disappear on addition of PIL (Table 1). The disappearance of nonpolar α phase is attributed to the highly polar nature of PIL. Further, intensity of bands at 1,400 and 1,430 cm^{-1} corresponding to CH$_2$ wagging observed in the spectra of pure blend decreases gradually and the band at 1,071 cm^{-1} for CF$_3$ out of plane deformation disappears with the addition of PIL. These alterations in the bands indicate conformational changes occurring in the GPE as these bands are highly sensitive to the conformational changes [28]. The spectra of GPE also show a new prominent band at 3,473 cm^{-1} which corresponds to –OH group. As expected, above observations show that imidazolium cation of PIL complexes with carbonyl group present in the blend through hydrogen bonding and crystalline phases present in the GPE are influenced by PIL. Other bands of the blend and PIL are found unmodified in the spectra of GPE.

SEM studies

Figure 2 shows SEM images of films of the blend and GPE with x=50, 60 and 70 wt%. It can be seen that the film of the pure blend has a compact granular surface morphology (Fig. 2a), and there is no visible segregation of the components participating in the blend formation which indicates good compatibility between PVdF-HFP and PVP. Grains of the blend are separated by clearly visible grain boundaries and very small pores. Average size of grains is found to be ~13 μm. In the GPE films, grains of the blend coalesce together to form bigger granules separated by bigger pores on addition of PIL into the blend matrix (Fig. 2b–d). The size of these granules is found to increase with increasing PIL concentration.

XRD studies

Figure 3 shows XRD patterns of the films of pure PVdF-HFP, blend, and GPE with x=50, 60, and 70 wt%. PVdF-HFP is a well-known semicrystalline polymer. The XRD pattern of PVdF-HFP shows two intense peaks at 18.6 and 20.3° and three low intensity peaks at 26.7, 39, and 44° (Fig. 3a). The first two peaks are superimposed over a broad halo from 11 to 24.7° showing partially amorphous nature of the polymer. The peaks at 18.6 and 26.7° belong to (100)+(020) and (021) reflections, respectively, of nonpolar crystalline phase (α phase) and the peak at 20.3° corresponds to (110) reflection

Fig. 2 SEM images (×1000) of the films of pure PVdF-HFP/PVP blend (**a**), PVdF-HFP/PVP + x wt% BMImHSO$_4$ with x=50 (**b**), 60 (**c**), and 70 (**d**)
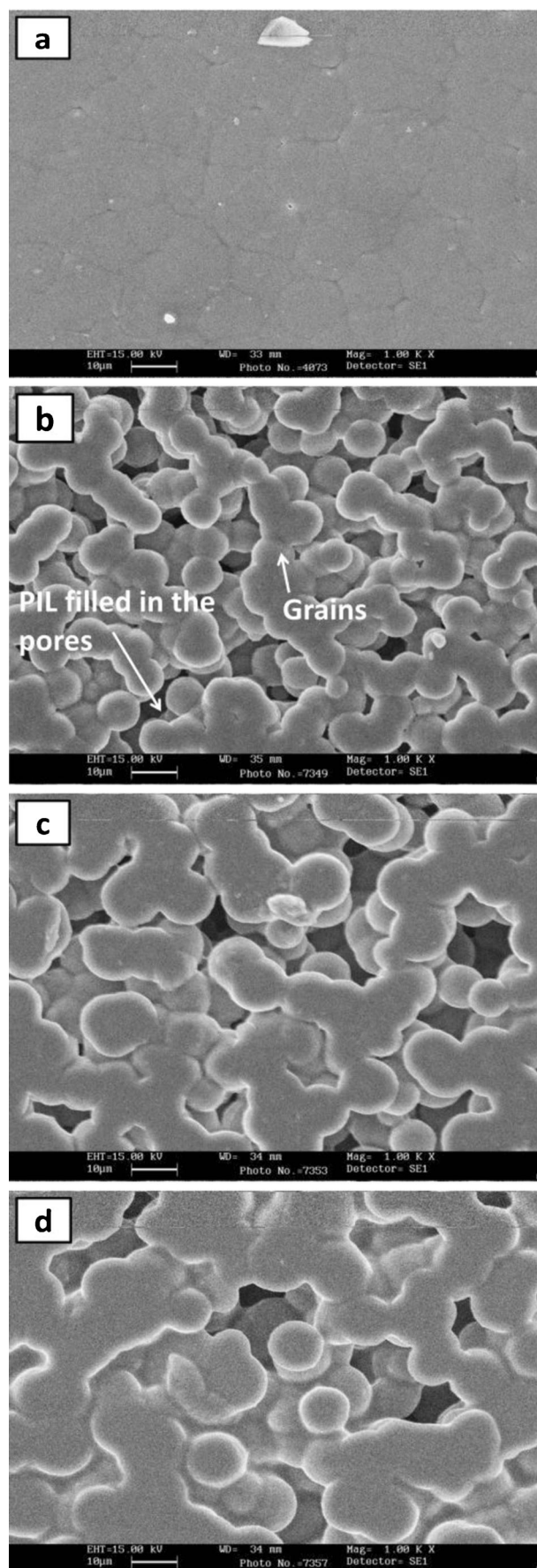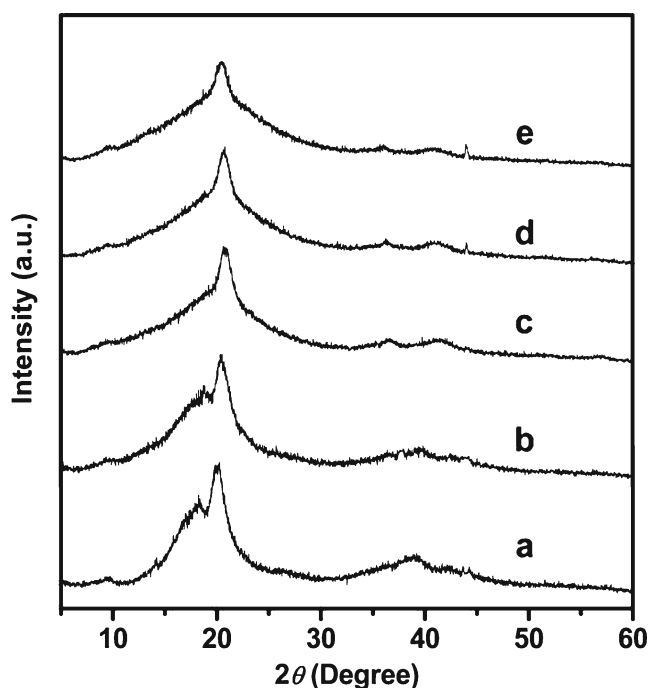
Fig. 3 XRD pattern of the films of pure PVdF-HFP (**a**), PVdF-HFP/PVP blend (**b**), PVdF-HFP/PVP + x wt% BMImHSO$_4$ with x=50 (**c**), 60 (**d**), and 70 (**e**)

of polar crystalline phase (γ phase) of PVdF-HFP [28]. In the XRD pattern of blend film, the peaks belonging to α and γ phases are found to be only slightly suppressed and shifted (Fig. 3b). This is attributed to the presence of amorphous PVP in the blend. The small changes observed may be due to small amount of PVP (10 wt%) in the blend. In the XRD patterns of
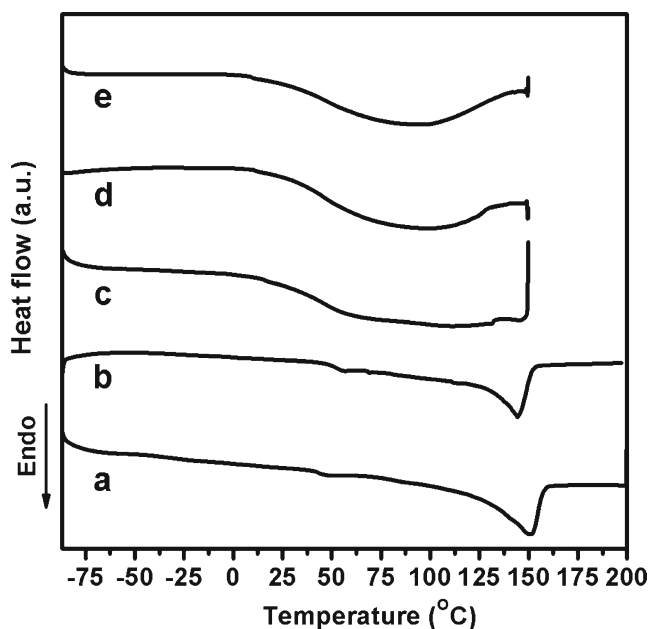
Fig. 4 DSC thermogram of the films of pure PVdF-HFP (**a**), PVdF-HFP/PVP blend (**b**), PVdF-HFP/PVP + x wt% BMImHSO$_4$ with x=50 (**c**), 60 (**d**), and 70 (**e**)

GPE films, peaks of α phase gradually disappear, and intensity of peak of γ phase gradually decreases (Fig. 3c–e). The halo observed in the XRD patterns also becomes broader with PIL concentration. These observations show decrease in crystallinity of the GPE on the addition of PIL. The disappearance of α phase and suppression of γ phase of PVdF-HFP in the GPE films have also been confirmed by the FTIR studies discussed above.

DSC studies

Figure 4 shows DSC patterns of the films of pure PVdF-HFP and blend in the temperature range –90 to 200 °C and of the films of GPE with x=50, 60, and 70 wt% in temperature range of –90 to 150 °C. The DSC thermogram of pure PVdF-HFP film shows an endothermic peak at ~151 °C which is attributed to melting of crystalline polymer matrix of PVdF-HFP (Fig. 4a). In the DSC pattern of blend film, this peak appears at a lower temperature (145 °C) which shows lowering of the melting point on blending (Fig. 4b). The DSC thermogram of the GPE film with x=50 wt% shows the endothermic peak corresponding to melting of the polymer at ~130 °C (Fig. 4c). This peaks further shifts to ~123 and 105 °C for GPE films with 60 and 70 wt% PIL, respectively. A new broad endothermic peak in the temperature range 27–123 °C is also observed in the DSC patterns of GPE film with x=50 wt%. This broad and asymmetric peak appears to consist of two peaks—a broad one with onset at ~27 °C and the other peaking at ~112 °C. As FTIR results show that GPE films contain adsorbed water, the broad peak is attributed to desorption of water from the GPE matrix on heating while the peak at 112 °C is attributed to melting of the semi-crystalline PVdF-HFP. Appearance of this melting peak shows presence of a new crystalline phase in the GPE along with the crystalline phase considered above that melts at 130, 123, and 105 °C in different GPE films. However, this new melting peak centered at 112 °C gradually disappears with increasing PIL concentration in the GPE leaving behind a broad water desorption peak. In order to confirm the presence of water in the GPE, DSC was carried out in cooling cycle between 150–25 °C and then in second heating cycle between 25–150 °C. The scans are shown in Fig. 5. It can be observed that in the second heating cycle, no endothermic peak appears between 27–123 °C. This shows that the initial endothermic peak observed in the first heating cycle corresponds to the water desorption and hence confirms presence of water in the GPE. Further, the DSC pattern taken in the cooling cycle shows an exothermic peak with an onset at ~140 °C. This peak may be attributed to recrystallization of PVdF-HFP. However, melting of the recrystallized phase could not be observed during the second heating cycle possibly because measurement was carried out only up to 150 °C.

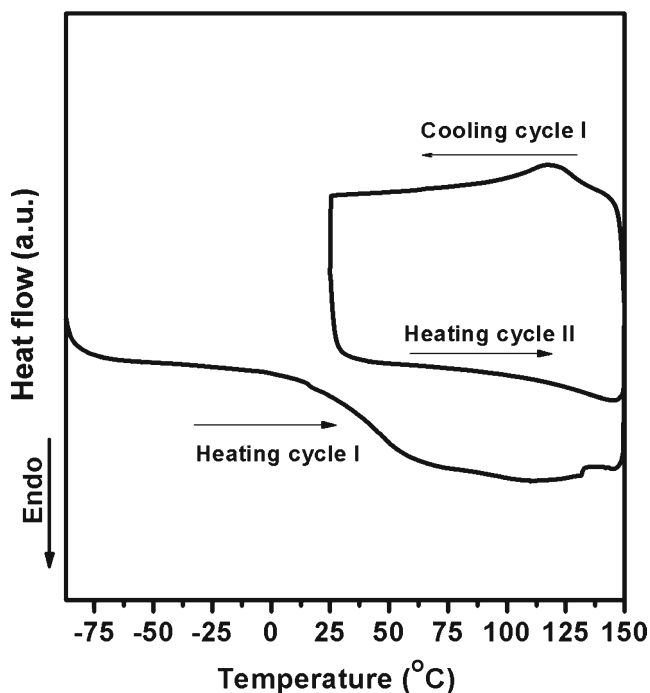As observed in the FTIR and XRD studies, blend films contain two crystalline phases—a nonpolar α phase and a

Fig. 5 DSC thermogram of the film of PVdF-HFP/PVP + 50 wt% BMImHSO$_4$ in heating and cooling cycles

polar γ phase of PVdF. As PIL is a highly polar salt, when it is added to the blend so as to obtain GPE films, it may affect α and γ phases differently owing to their nonpolar and polar nature, respectively. Therefore, interchain attraction in the nonpolar α phase is likely to be weakened more as compared to that in the polar γ phase. Therefore, we may expect two separate melting points corresponding to these phases. Moreover, as observed in FTIR and XRD results, α phase of PVdF-HFP gradually disappears from the blend on addition of PIL; therefore, we may attribute the peak at 112 °C to the melting of α phase. The γ phase is also affected by the addition of PIL as its melting temperature decreases from 130 °C for GPE film with 50 wt% PIL to 123 and 105 °C for GPE films with 60 and 70 wt% PIL. We could not observe any peak corresponding to glass transition temperature of the pure PVdF-HFP, blend, and GPE in the temperature range of measurement. It may be because of less sensitivity of DSC setup.

Ionic conductivity

Ionic conductivity of the GPE films was evaluated using Nyquist plots as shown in Fig. 6. Ionic conductivity of the films has been calculated using the equation $\sigma = d / R_b A$, where d is thickness of the electrolyte membrane, A is area of the electrode, and R_b is the bulk resistance obtained from the intercept of spikes with the real axes of the Nyquist plot. The ambient (RT=30 °C, RH=60 %) ionic conductivity of the films with 50, 60, and 70 wt% PIL was obtained as 1.1×10^{-3}, 2.2×10^{-3}, and 3.9×10^{-3} S cm^{-1}, respectively which is

comparable to the ionic conductivity of the pure PIL ($\sim 1 \times 10^{-3}$ S cm^{-1}). This is attributed to the highly porous structure of the films as observed in the SEM images. The slightly higher conductivity than pure PIL may be due to adsorbed water in the GPE films. The GPE films with PIL concentration more than 70 wt% could not be considered for investigations as they had poor dimensional stability and had a "glue-like" appearance. It can be seen that the conductivity of the GPE films increases with the increasing content of PIL in the polymer. This enhancement can be explained on the basis of the "two-phase model" described by Saito et al. [34]. The ion conduction in the GPE films may be expected to occur through the liquid phase (IL) trapped in the pores and also through the PVdF-HFP/PVP blend gel phase. In the gel phase, ion conduction occurs via interaction between IL and the polymer matrix in which ion–ion interaction, ion–polymer interaction, and amorphicity play a significant role. On the other hand, the liquid phase trapped in the pores of the blend gel supports high ionic mobility. As observed in XRD and SEM studies, amorphicity and pore size of films increase with the concentration of PIL; therefore, ion conduction through both the phases gets enhanced which leads to the enhancement in ionic conductivity with increasing PIL concentration in the GPE films.

Figure 7 shows temperature dependence of ionic conductivity of GPE films of different compositions measured in the temperature range 30–130 °C. It can be seen that ionic conductivity of the film with 50 wt% PIL follows the Arrhenius-type thermally activated process, which is typical of a semi-crystalline polymer electrolyte in which ion conductivity is
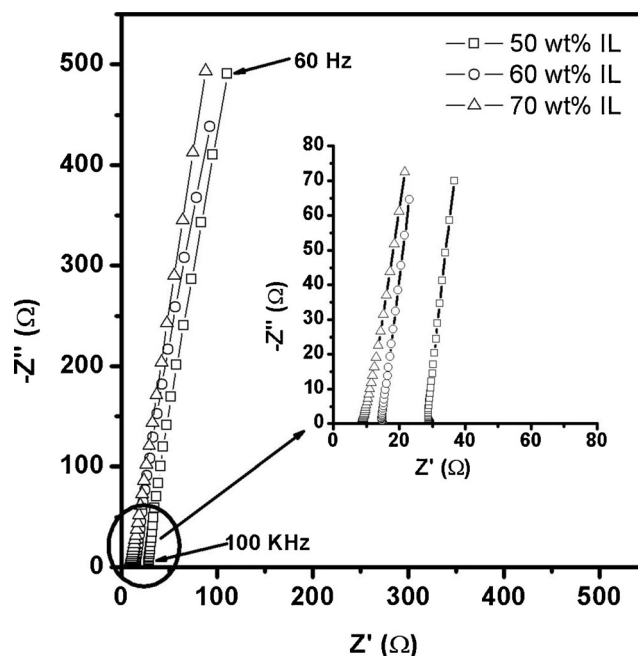

Fig. 6 Nyquist plots of SS/GPE/SS cells with different concentrations of IL in GPE
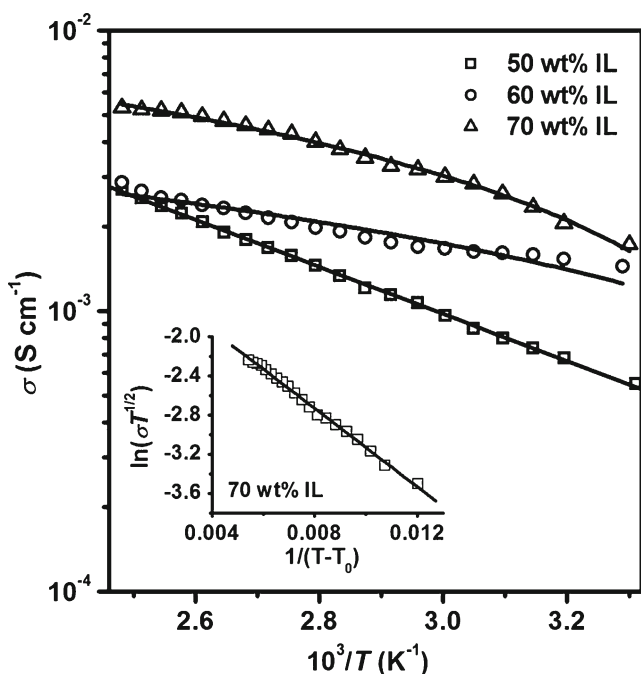
Fig. 7 Temperature dependence of ionic conductivity of PVdF-HFP/PVP + x wt% BMImHSO$_4$ GPE films

driven by the movement of thermally activated ions through the polymer matrix via polymer segmental motion. On the other hand, with 60 and 70 wt% IL, the conductivity follows Vogel–Tamman–Fulcher (VTF) behavior with temperature. Clearly, the transport mechanism is dependent on PIL concentration in the GPE films. As already described, ion conduction in GPE films may be expected to occur through the liquid phase (PIL) entrapped in the pores and also through assistance of polymer chains forming the solid skeleton of GPE. It may therefore be conjectured that in GPE film with low concentration of PIL (50 wt%), ion conduction occurred predominantly through the assistance of polymer chains giving rise to the variation typical of semicrystalline polymer electrolytes; however, for high concentration of IL, i.e., for 60 and 70 wt% of IL in the blend, conduction through the liquid phase shows its dominance giving rise to VTF behavior with temperature. Activation energy for the film with 50 wt% PIL has been calculated using the Arrhenius equation:

$$\sigma = \sigma_o \exp\left(\frac{-E_a}{k_b T}\right) \qquad (1)$$

where E_a is the activation energy, σ_o is a pre-exponential factor, and k_b is the Boltzmann constant. The activation energy of the above composition is obtained as ~0.16 eV. The VTF behavior of conductivity variation for the GPE films with 60 and 70 wt% PIL is governed by the equation,

$$\sigma = A T^{-\frac{1}{2}} \exp\left(\frac{-B}{T-T_o}\right) \qquad (2)$$

where the parameter B is associated with rate at which viscosity of the system changes with temperature, A is a constant which signifies conductivity at infinitely high temperature, and T_o represents temperature close to the glass transition temperature. For the film with 70 wt% PIL, values of A, B, and T_o, obtained by nonlinear curve fitting of the experimental data with the VTF equation, are 0.32 S cm^{-1} K$^{1/2}$, 462 J mol^{-1}, and 220 K, respectively. It may also be noted from the variation of ionic conductivity with temperature that the GPE films immobilizing BMImHSO$_4$ PIL are thermally stable up to 130 °C as they do not lose conductivity due to possible electrolyte leakage.

Confirmation of proton transport and electrochemical stability window

One of the major challenges with proton-conducting solid electrolytes is to ascertain protonic transport. For electrolytes like sodium and lithium ion conductors, transport number measurements can be conveniently carried out because of availability of suitable reversible electrodes. However, due to nonavailability of such solid electrodes for proton-conducting materials, techniques like fuel cell test, solid-state proton NMR, and coulometry have been used by several authors for confirming the proton conduction in polymer electrolytes [16, 35, 36]. In the present work, we have used complex impedance spectroscopy and cyclic voltammetric studies to confirm the proton conduction in the GPE films.

A mixture of Zn and ZnSO$_4$.7H$_2$O has been used as anode by several workers in proton batteries. The mixture has been described to act as a proton source by giving following reaction [20]:

$$\eta Zn + ZnSO_4.7H_2O \rightleftarrows Zn_{\eta+1}SO_4.(7-\eta)H_2O.2\eta OH \qquad (3)$$
$$+ 2\eta H^+ + 2\eta e^-$$
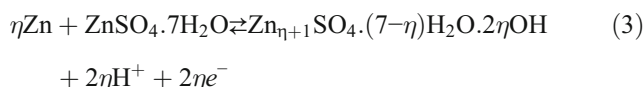
Therefore, we may choose Zn + ZnSO$_4$.7H$_2$O as a reversible electrode in the case of proton-conducting electrolytes. Hence, in the proposed scheme of measurement, we have carried out complex impedance and CV measurements on the following symmetrical cells:

Cell-1:   SS |GPE film| SS and
Cell-2:   Zn + ZnSO$_4$.7H$_2$O |GPE film| Zn + ZnSO$_4$.7H$_2$O

The GPE film with 70 wt% PIL has been used as electrolyte in both the cells as this composition has the highest ionic conductivity. In cell-1, SS acts as a blocking electrode. Figure 8 shows the comparative impedance plots for cell-1 and cell-2. The impedance response of cell-1 shows only a near-vertical spike parallel to the imaginary axis of the complex impedance plot (Fig. 8a) while that of cell-2 shows an almost well-defined semicircle as a function of frequency in the
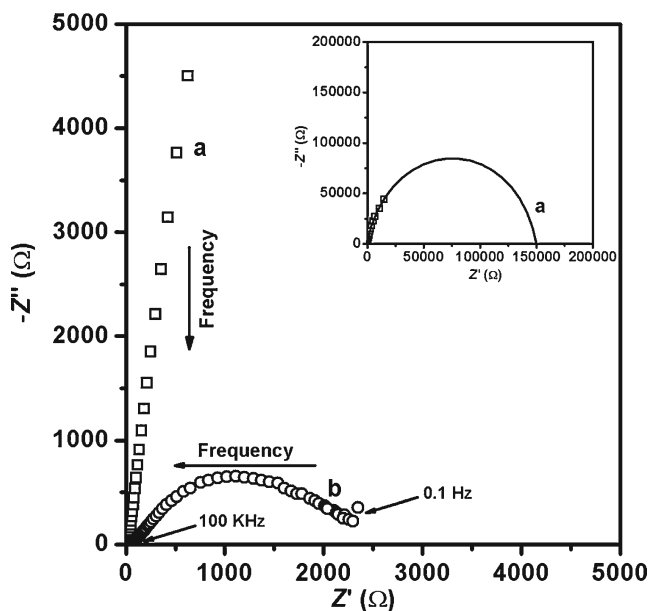
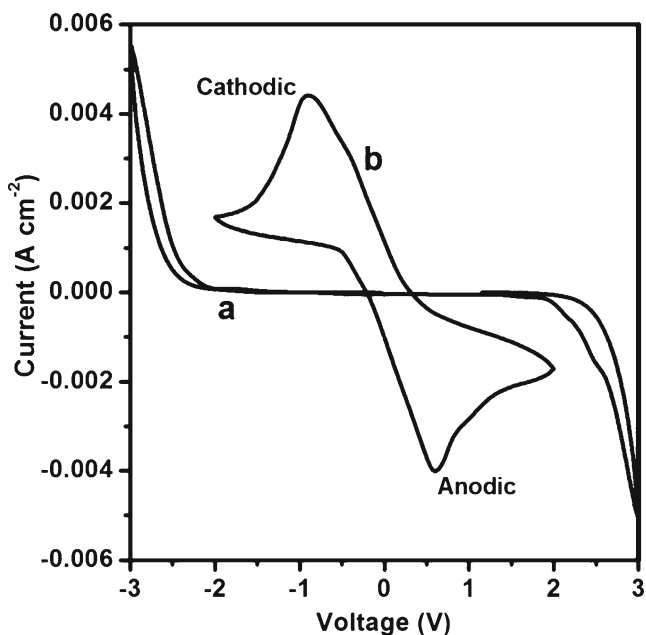**Fig. 8** AC impedance plots for cell-1: SS |PVdF-HFP/PVP + 70 wt% BMImHSO₄ GPE film| SS (**a**) and cell-2: Zn + ZnSO₄.7H₂O |PVdF-HFP/PVP + 70 wt% BMImHSO₄ GPE film| Zn + ZnSO₄.7H₂O (**b**). *Inset*: AC impedance plot of cell-1 from 0.1 Hz to 100 kHz

complex impedance plot (Fig. 8b). The near-vertical spike observed in the case of cell-1 confirms the blocking nature of the SS electrodes, while the semicircular complex impedance plot observed for cell-2 confirms proton conduction in the GPE film as $Zn + ZnSO_4.7H_2O$ acts as a reversible electrode (proton source). The bulk resistance (R_b) of GPE film and the electrode-electrolyte interfacial resistance ($R_{interface}$) have been obtained from the intercept of high frequency and low

Fig. 9 Cyclic voltammogram for cell-1: SS |PVdF-HFP/PVP + 70 wt% BMImHSO₄ GPE film| SS (**a**) and cell-2: Zn + ZnSO₄.7H₂O |PVdF-HFP/PVP + 70 wt% BMImHSO₄ GPE film| Zn + ZnSO₄.7H₂O (**b**)
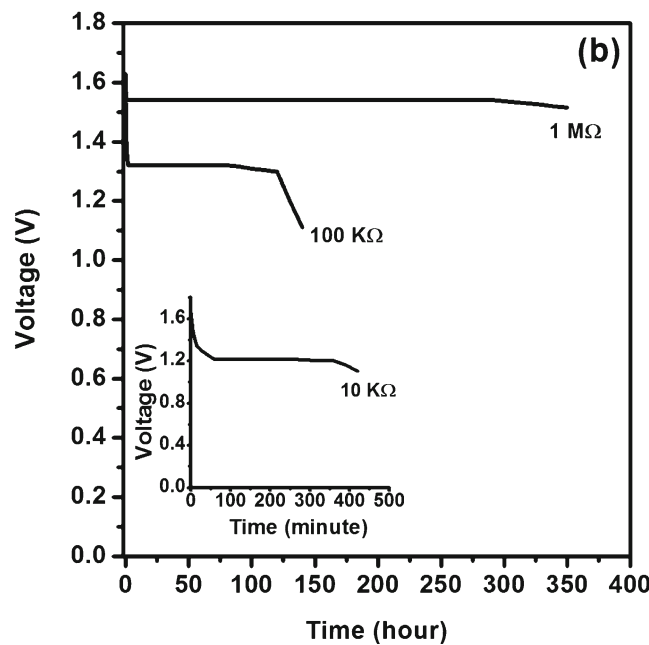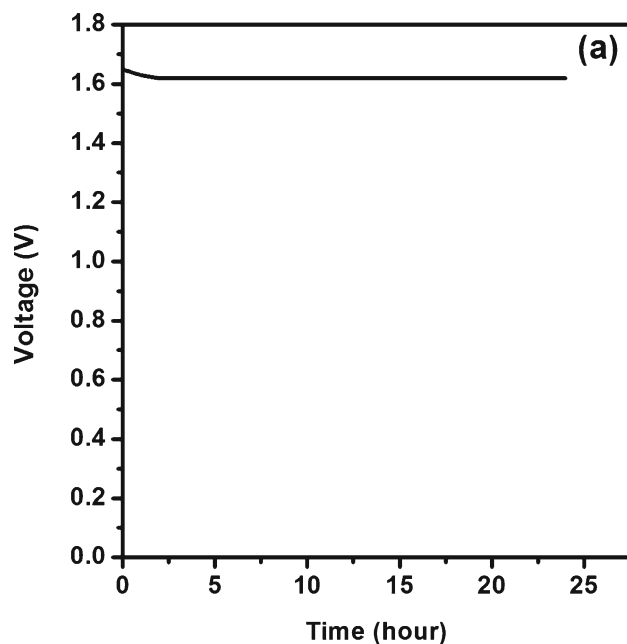

Fig. 10 Open circuit voltage (OCV) as a function of time (**a**) and discharge characteristics at different loads (**b**) of the Zn + ZnSO₄.7H₂O |PVdF-HFP/PVP + 70 wt% BMImHSO₄ GPE film| PbO₂ + V₂O₅ cell

frequency impedance curves on the real axis (Z'-axis) of the impedance plot, respectively. The values of R_b have been found to be approximately same lying between ~30–47 Ω cm² for cell-1 and cell-2. The value of $R_{interface}$ is found to be ~2.4 kΩ for $Zn + ZnSO_4.7H_2O$/GPE interface in cell-2. However, the value of $R_{interface}$ has been obtained as ~150 kΩ for SS/GPE interface in cell-1(inset, Fig. 8). The substantially low value of $R_{interface}$ in the case of $Zn + ZnSO_4.7H_2O$/GPE interface is attributed to the equilibrium established between the proton source ($Zn + ZnSO_4.7H_2O$ electrode) and protons (H^+ ions) in
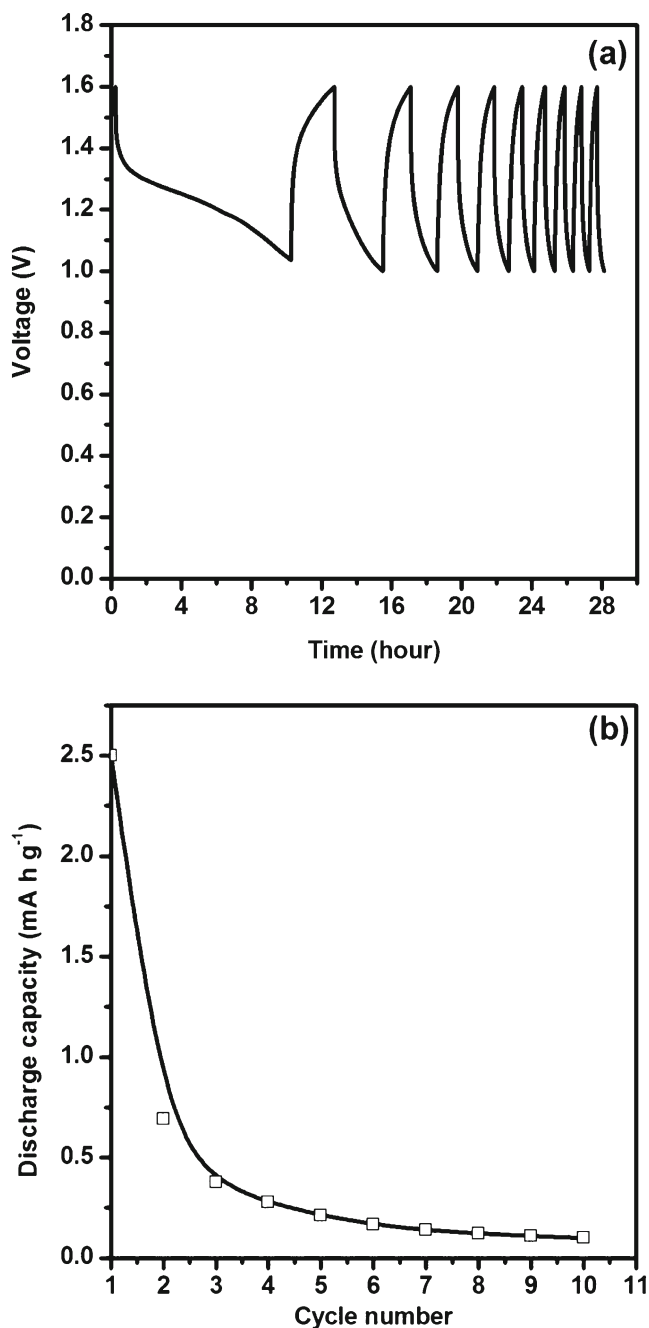
Fig. 11 Charge–discharge curve (a) and discharge capacity (b) of the Zn+ZnSO$_4$.7H$_2$O |PVdF-HFP/PVP + 70 wt% BMImHSO$_4$ GPE film| PbO$_2$ + V$_2$O$_5$ cell

the GPE film while higher value of $R_{interface}$ in the case of SS/GPE further indicates the ion blocking nature of SS. Above observations establish protonic conduction in the GPE film.

Protonic conduction in the GPE films has been further confirmed by comparative CV study of cell-1 and cell-2. The CV plots for the cells obtained at scan rate of 5 mV s^{-1} are shown in Fig. 9. The plot shows distinct cathodic and anodic current peaks for cell-2 (Fig. 9b), whereas no such features are observed for cell-1 (Fig. 9a). The anodic and

cathodic peaks present in the voltammogram of cell-2 are separated by ~1.2 V, which may be due to the use of two electrodes geometry with no reference electrode [3, 4, 37]. It may be noted that the magnitude of currents in the cell-2 is several times larger than that in the cell-1. These observations suggest protonic oxidation and reduction taking place at the respective electrode-electrolyte interfaces of the cell-2 which further confirms protonic conduction in the GPE film.
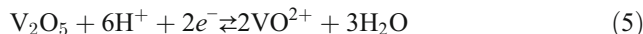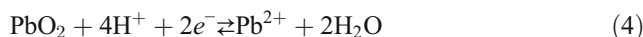
The electrochemical stability window (ESW) indicates working voltage range of electrolyte films which is an important parameter for their applications in electrochemical devices. The measurement of working voltage range for GPE films with 50, 60, and 70 wt% PIL was carried out by cyclic voltammetry on the SS/GPE film/SS cell. The voltammograms show identical stability pattern for all the films. A typical cyclic voltammogram is shown in Fig. 9a for GPE film with 70 wt% PIL. In order to evaluate the ESW, the cut-off potentials were chosen on those points from where the resulting currents start rising abruptly. In the present case, the potential range is found to be ±1.9 V. This gives ESW for the film as ~3.8 V. The ESW measurement was carried out for GPE film with 70 wt% PIL with scan rates of 2, 10, 15, and 30 mV s^{-1} also. In each case, ESW has been found to be ~3.8 V.
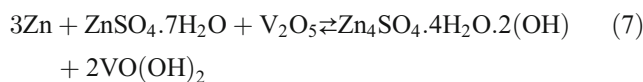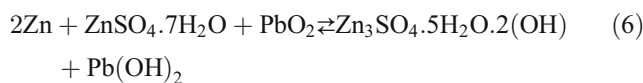
Battery characteristics

In order to examine the performance of the GPE films as electrolyte in the proton battery, the highest conducting composition (blend+70 wt% PIL) of the GPE has been employed to fabricate the cell with the configuration Zn + ZnSO$_4$.7H$_2$O (anode) |PVdF-HFP/PVP + 70 wt% BMImHSO$_4$ GPE film| PbO$_2$ + V$_2$O$_5$ (cathode). The cell chemistry may be understood as below:

In proton batteries, at anode, oxidation of Zn produces Zn^{2+} ions and electrons. While electrons flow in the external circuit, the Zn^{2+} ions are left at the anode. During discharge cycle of the battery, protons are supplied by the hydrated zinc sulphate. The complete anodic reaction can be given by Eq. 3.

At the positive electrode (cathode), reduction of PbO$_2$ and V$_2$O$_5$ occurs according to the following reactions during the cell process [38]:

$$PbO_2 + 4H^+ + 2e^- \rightleftarrows Pb^{2+} + 2H_2O \qquad (4)$$

$$V_2O_5 + 6H^+ + 2e^- \rightleftarrows 2VO^{2+} + 3H_2O \qquad (5)$$

Thus, the complete cell reactions may be given as:

$$2Zn + ZnSO_4.7H_2O + PbO_2 \rightleftarrows Zn_3SO_4.5H_2O.2(OH) \qquad (6)$$
$$+ Pb(OH)_2$$

$$3Zn + ZnSO_4.7H_2O + V_2O_5 \rightleftarrows Zn_4SO_4.4H_2O.2(OH) \qquad (7)$$
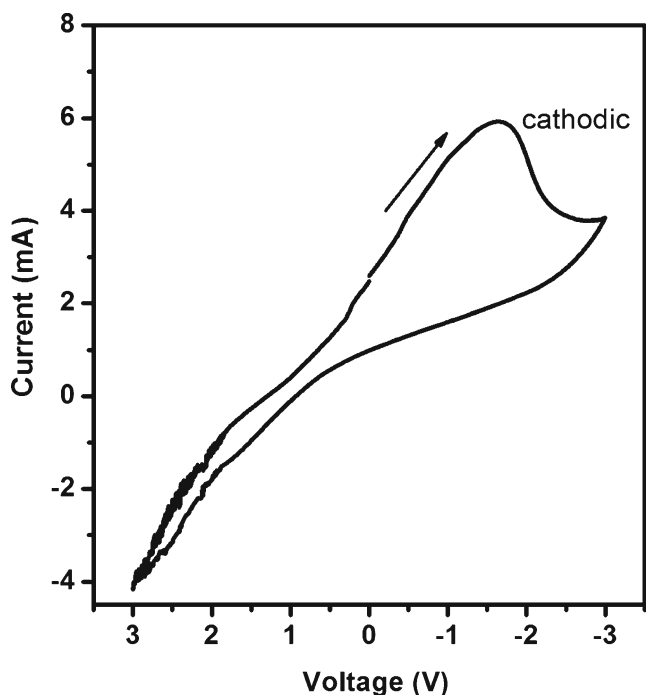$$+ 2VO(OH)_2$$

Fig. 12 Cyclic voltammogram of the Zn + ZnSO₄.7H₂O |PVdF-HFP/ PVP + 70 wt% BMImHSO₄ GPE film| PbO₂ + V₂O₅ cell

Figure 10a shows voltage response of the cell as a function of time in open circuit conditions. The plot shows the cell to be reasonably stable in the open circuit condition. The open circuit voltage (OCV) of the cell has been found to be 1.62 V. This value is slightly less than the theoretical value of OCV of the cell which is expected to be ~1.7188 V as the standard oxidation potential of Zn is $E^{O'}_{ox} = -0.7618$ V and reduction potential of V_2O_5 is $E^{O'}_{red} = 0.957$ V. The difference between theoretical and the experimental values of OCV may be attributed to the possible reduction of ZnSO₄·7H₂O ($E^{O'}_{red}$ ~0.7993 V) at the anode along with oxidation of Zn which reduces the overall electrode potential of anode [26]. Therefore, the OCV of the cell is expected to be less than the theoretical value. It may be noted that the reduction potential of V_2O_5 has been taken as standard over the reduction potential of PbO₂ ($E^{O'}_{red} = 1.455$ V). Figure 10b shows discharge

characteristics of the battery at 1 MΩ, 100 kΩ, and 10 kΩ loads. Each cell was stabilized in the open circuit condition for ~5 h before discharge. It can be seen that before reaching discharge plateau, each cell shows a small voltage drop. This may be due to activation polarization, which occurs when rate of an electrochemical reaction at electrode surface is controlled by sluggish electrode kinetics [27, 39]. It is further observed that at 1 MΩ load, the cell remains stable at 1.54 V for ~300 h and provides an energy density of 35.2 W h kg⁻¹. However, at the load, 100 kΩ, cell remains stable only up to ~100 h and gives an energy density of 11.3 W h kg⁻¹. The discharge time further reduces when cell is discharged through 10 kΩ load as shown in Fig. 9b (inset). In this case, the energy density is obtained as ~2.9 W h kg⁻¹. Above observations show that performance of the battery is comparatively better at low current drain.

Figure 11a shows rechargeability of the cell tested in potential range 1.0–1.6 V at a current of 50 μA for 10 cycles. The cell was found to go through quick charge/discharge after the first cycle. A plot of the discharge capacity of the cell versus number of cycles is shown in Fig. 11b. It may be observed that after the first discharge cycle, discharge capacity of the cell fades away significantly. The discharge capacity of the cell has been obtained as 1.6 mA h g⁻¹ for the first discharge cycle which decreases to 0.1 mA h g⁻¹ after ten cycles. The calculation of discharge capacity has been done with respect to weight of the active cathode material PbO₂ + V₂O₅. For a rechargeable cell, reversibility, i.e., intercalation and de-intercalation of the ions at the cathode is a primary requirement. Therefore, poor rechargeability shown by the cell may be associated with the poor reversibility of the cathode. In order to check reversibility of the cathode, cyclic voltammetry of the fabricated battery has been carried out. The obtained voltammogram is shown in Fig. 12. It can be seen that only cathodic peak is visible at −1.6 V corresponding to the proton deposition at the cathode, however no anodic peak is observed in the reverse scan. The nonappearance of the anodic peak indicates almost nonreversibility of the positive electrode. Structural changes in the cathode materials and poor electrode-electrolyte interfacial stability are the possible

Table 2 Open circuit voltage (OCV) and energy density of proton batteries

Cell configurations	OCV (V)	Energy density (W h kg⁻¹)	References
Zn + ZnSO₄·7H₂O |[{(PMMA + PVdF-HFP) + xSiO₂} + NH₄SCN in EC + PC}] GPE| PbO₂ + V₂O₅ + C + electrolyte	1.55	6.11	[5]
Zn + ZnSO₄·7H₂O + MHx |PEO: NH₄ClO₄ + PC| V₂O₅ + PbO₂ + C + E	1.57	0.56	[21]
Zn + ZnSO₄·7H₂O + MHx |55 % PMA + 45 %APT| V₂O₅ + PbO₂ + C + E	1.50	0.735	[23]
Zn + ZnSO₄·7H₂O |PEO: NH₄HSO₄ + SiO₂| PbO₂ + V₂O₅ + C	1.50	0.122	[24]
Zn + ZnSO₄·7H₂O |80PVA:20NH₄NO₃| V₂O₅ + PbO₂ + PEC	1.89	7.9	[25]
Zn + ZnSO₄·7H₂O |[(PVdF-HFP)/PVP] + 70 wt% BMImHSO₄| PbO₂ + V₂O₅ + C + electrolyte	1.62	35.2	Present work

reasons behind the capacity loss, which need further investigations for improving the cell performance.

A comparison of the performance parameters of the proton battery presented in this paper with those of pre-existing proton batteries is given in Table 2. It may be remarked that the performance of the proton battery having BMImHSO$_4$ PIL-based GPE film studied in this paper shows better results as compared to previously reported proton batteries.

Conclusions

Free-standing proton-conducting GPE films of 90 wt% PVdF-HFP/10 wt% PVP + x BMImHSO$_4$, (x=50, 60, and 70 wt%) have been prepared by solution-cast technique. Films show enhanced porosity and amorphicity and ionic conductivity close to that of pure protic ionic liquid in the given compositional range. The GPE film has been used to fabricate proton battery. The battery shows enhanced performance parameters with the PIL-based GPE used as electrode separating membrane and ion conductor. The battery shows rechargeability for 10 cycles but discharge capacity of the cell fades away quickly after the first cycle, which is possibly due to the poor reversibility of the positive electrode.

References

1. Song JY, Wang YY, Wan CC (1999) J Power Sources 77:183–197
2. Stephan M (2006) Eur Polym J 42:21–42
3. Sellam, Hashmi SA (2012) J Solid State Electrochem 16:3105–3114
4. Kumar D, Hashmi SA (2010) J Power Sources 195:5101–5108
5. Mishra K, Hashmi SA, Rai DK (2013) J Solid State Electrochem 17:785–793
6. Kumar A, Gupta RK (2002) Fundamentals of polymer engineering. Marcel Dekkar Inc, New York
7. Chen NP, Hong L (2002) Polymer 43:1429–1436
8. Hahn BR, Schönherr OH, Wendorff JH (1987) Polymer 28:201–208
9. Qiao JL, Hamaya T, Okada T (2005) Polymer 46:10809–10816
10. Wang Z, Tang Z (2003) Mater Chem Phys 82:16–20
11. Ohno H (2005) Electrochemical aspects of ionic liquids. Wiley, Hoboken
12. Greaves TL, Drummond CJ (2008) Chem Rev 108:206–237
13. Anouti M, Caravanier MC, Floch CL, Lemordant D (2008) J Phys Chem B 112:9406–9411
14. Johnson KE, Pagni RM, Bartmess J (2007) Monatsh Chem 138:1077–1101
15. Nakamoto H, Noda A, Hayamizu K, Hayashi S, Hamaguchi H, Watanabe M (2007) J Phys Chem C 111:1541–1548
16. Ogihara W, Kosukegawa H, Ohno H (2006) Chem Commun 34:3637–3639
17. Fernicola A, Penero S, Scrosati B, Tamada M, Ohno H (2007) Chem Phys Chem 8:1103–1107
18. Fernicola A, Penero S, Scrosati B (2008) J Power Sources 178:591–595
19. Martinelli A, Matic A, Jacobsson P, Borjesson J, Fernicola A, Panero S, Scrosati B, Ohno H (2007) J Phys Chem B 111:12462–12467
20. Guitton J, Dongui B, Mosdale R, Forestier M (1988) Solid State Ionics 28–30:847–852
21. Pratap R, Singh B, Chandra S (2006) J Power Sources 161:702–706
22. Pandey K, Lakshmi N, Chandra S (1998) J Power Sources 76:116–123
23. Lakshmi N, Chandra S (2002) J Power Sources 108:256–260
24. Agrawal RC, Hashmi SA, Pandey GP (2007) Ionics 13:295–298
25. Selvasekarapandian S, Hema M, Kawamura J, Kamishima O, Baskaran R (2010) J Phys Soc Jpn 79:163–168
26. Ali AMM, Mohamed NS, Arof AK (1998) J Power Sources 74:135–141
27. Ng LS, Mohamad AA (2006) J Power Sources 163:382–385
28. Abbrent S, Plestil J, Hlavata D, Lindgren J, Tegenfeldt J, Wendsjö A (2001) Polymer 42:1407–1416
29. Du CH, Zhu BK, Xu YY (2006) J Mater Sci 41:417–421
30. Jeon Y, Sung J, Seo C, Lim H, Cheong H, Kang M, Moon B, Ouchi Y, Kim D (2008) J Phys Chem B 112:4735–4740
31. Kiefer J, Fries J, Leipertz A (2007) Appl Spectrosc 61:1306–13011
32. Malek K, Puc A, Schroeder G, Rybachenko VI, Proniewicz LM (2006) Chem Phys 327:439–451
33. Talaty ER, Raja S, Storhaung VJ, Doll A, Carper WR (2004) J Phys Chem B 108:13177–13184
34. Saito Y, Kataoka H, Quartarone E, Mustarelli P (2002) J Phys Chem B 106:7200–7204
35. Hashmi SA, Kumar A, Maurya KK, Chandra S (1990) J Phys D Appl Phys 23:1307–1314
36. Selvasekarapandian S, Hirankumar G, Kawamura J, Kuwata N, Hattori T (2005) Mater Lett 59:2741–2745
37. Munichandraiah N, Scanlon LG, Marsh RA, Kumar B, Sircar AK (1995) J Appl Electrochem 25:857–863
38. Vanysek P (2000) Electrochemical series. CRC Press, Boca Raton
39. Broadhead J, Kuo HC (2001) In: Linden D, Reddy TB (eds) Handbook of batteries, 3rd edn. McGraw-Hill, New York, p 21